Draft version October 14, 2019
Typeset using LaTeX **twocolumn** style in AASTeX62

2-OGC: Open Gravitational-wave Catalog of binary mergers from analysis of public Advanced LIGO and Virgo data

Alexander H. Nitz,[1,2] Thomas Dent,[3] Gareth S. Davies,[3] Sumit Kumar,[1,2] Collin D. Capano,[1,2] Ian Harry,[4,5] Simone Mozzon,[4] Laura Nuttall,[4] Andrew Lundgren,[4] and Marton Tápai[6]

[1]*Max-Planck-Institut für Gravitationsphysik (Albert-Einstein-Institut), D-30167 Hannover, Germany*
[2]*Leibniz Universität Hannover, D-30167 Hannover, Germany*
[3]*Instituto Galego de Física de Altas Enerxías, Universidade de Santiago de Compostela, 15782 Santiago de Compostela, Galicia, Spain*
[4]*University of Portsmouth, Portsmouth, PO1 3FX, United Kingdom*
[5]*Kavli Institute of Theoretical Physics, UC Santa Barbara, CA*
[6]*Department of Experimental Physics, University of Szeged, Szeged, 6720 Dóm tér 9., Hungary*

ABSTRACT

We present the second Open Gravitational-wave Catalog (2-OGC) of compact-binary coalescences, obtained from the complete set of public data from Advanced LIGO's first and second observing runs. For the first time we also search public data from the Virgo observatory. Our analysis is based upon updated methods to improve detection of compact binary mergers by incorporating corrections for short time variations in the detectors' noise power spectral density and instantaneous network sensitivity. We identify a population of 14 binary black hole mergers with $p_{\rm astro} > 0.5$ along with the GW170817 binary neutron star merger. We confirm the binary black hole merger observations of GW170121, GW170304, and GW170727. We also report GW151205, a new marginal binary black hole merger during the first observing run. No other individually significant binary neutron star candidates are found, nor did we observe any significant neutron star–black hole candidates. We make available our comprehensive catalog of events, including the sub-threshold population of candidates to enable deeper follow-up as our understanding of the underlying populations evolves.

Keywords: gravitational waves — neutron stars — black holes — compact binary stars

1. INTRODUCTION

The Advanced LIGO (Aasi et al. 2015) and Virgo (Acernese et al. 2015) observatories have ushered in the age of gravitational-wave astronomy. The first and second observing runs (O1 and O2) of Advanced LIGO and Virgo covered the period from 2015-2017. This provided a total of 171 days of multi-detector observing time. To date, these instruments have observed a population of binary black holes and a single binary neutron star, GW170817, which has become one of the most observed astronomical events (Abbott et al. 2017a). Ten binary black hole mergers and a single binary neutron star merger have been reported in this period by the LIGO and Virgo Collaborations (Abbott et al. 2019a). Several independent analyses have examined publicly released data (Nitz et al. 2019a; Antelis & Moreno 2018; Venumadhav et al. 2019a), including an analysis targeting binary black hole mergers that reported several additional candidates (Venumadhav et al. 2019b).

The first open gravitational-wave catalog (1-OGC) searched for compact-binary coalescences during O1 (Nitz et al. 2019a). We extend that analysis to cover both O1 and O2 while incorporating Virgo data for the first time. During the first observing run, only the two LIGO instruments were observing. Joint three-detector observing with the Virgo instrument began in August 2017 during the second observing run.

We make additional improvements to our search by accounting for short-time variations in the network sensitivity and power spectral density (PSD) estimates directly in our ranking of candidate events. A similar procedure for tracking PSD variations was independently developed in Venumadhav et al. (2019a,b); Zackay et al. (2019). We produce a comprehensive catalog of candidate events from our matched-filter search which covers binary neutron star (BNS), neutron star – black

Corresponding author: Alexander H. Nitz
alex.nitz@aei.mpg.de

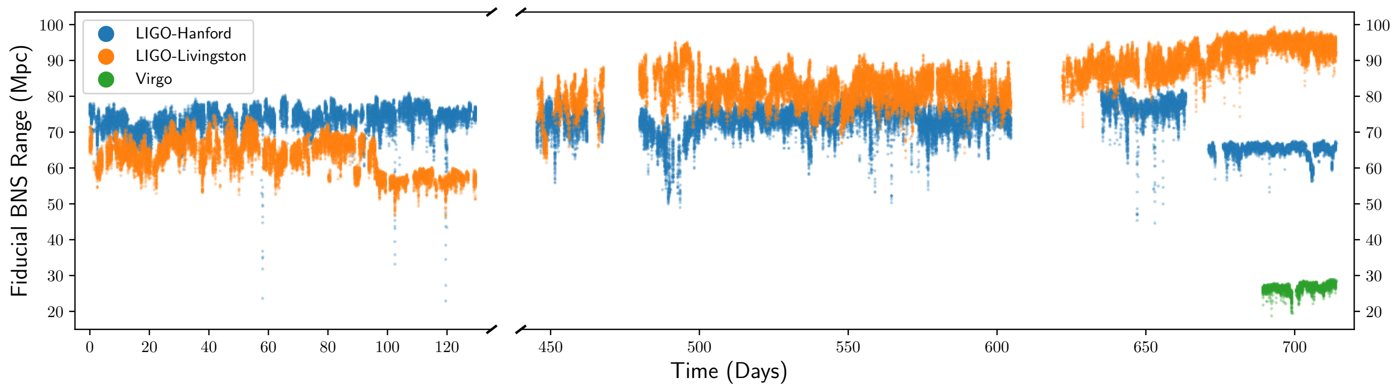

Figure 1. The sky- and orientation-averaged distance up to which each observatory can detect a 1.4-1.4$M_\odot$BNS merger with expected SNR equal to 8 over the O1 and O2 observing runs. The Virgo observatory did not participate in the first observing run, but joined towards the end of the second observing run.

hole (NSBH), and binary black hole (BBH) mergers[1]. While not individually significant on their own, sub-threshold candidates can be correlated with gamma-ray bursts (Nitz et al. 2019b), high-energy neutrinos (Countryman et al. 2019), optical transients (Andreoni et al. 2018; Setzer et al. 2018), and other counterparts to uncover new, fainter sources.

In addition to our broad search, we conduct a targeted analysis to uncover fainter BBH mergers. It is possible to confidently detect binary black hole mergers which are not individually significant in the context of the wider search space by considering their consistency with the population of confidently observed binary black hole mergers. The collection of highly significant detected events constrains astrophysical rates and distribution with relatively small uncertainties (Abbott et al. 2019b). For this reason, we do not yet employ this technique for binary neutron star or neutron star–black hole populations, as their rates and mass and spin distributions are much less constrained. We improve over the BBH focused analysis introduced in Nitz et al. (2019a) by considering an explicit population prior (Dent & Veitch 2014). This focused approach is most directly comparable to the results of (Venumadhav et al. 2019b), which considers only binary black hole mergers, rather than a broad parameter search such as employed in Abbott et al. (2019a).

We find 8 highly significant binary black hole mergers at false alarm rates less than 1 per 100 years in our full analysis along with the binary neutron star merger, GW170817. No other individually significant BNS or NSBH sources were identified. However, if the population of these sources were to be better understood, it may be possible to pick out fainter mergers from our population of candidates. When we apply a ranking to search candidates that optimizes search sensitivity for a population of BBH mergers similar to that already detected, we identify a further 6 such mergers with a probability of astrophysical origin above 50%. These include GW170818 and GW170729 which were reported in Abbott et al. (2019a) along with GW170121, GW170727, and GW170304 which were reported in Venumadhav et al. (2019b). We report one new marginal BBH candidate, GW151205. Our results are broadly consistent with both Venumadhav et al. (2019b) and Abbott et al. (2019a).

[1] www.github.com/gwastro/2-ogc

2. LIGO AND VIRGO OBSERVING PERIOD

We analyze the complete set of public LIGO and Virgo data (Vallisneri et al. 2015). The distribution of multi-detector analysis time and the evolution of the observatories' sensitivities over time is shown in Table 1 and

Table 1. Observing time in days for different instrument observing combinations. We use here the abbreviations H, L, and V for the LIGO-Hanford, LIGO-Livingston, and Virgo observatories respectively. Note, some data may not be analyzed due to analysis constraints. Only the indicated combination of observatories were operating for each time period, hence each is exclusive of all others.

Observing	Time(days)
H	65.4
L	50.0
V	1.7
HL	151.8
LV	2.2
HV	1.7
HLV	15.2

Fig. 1 respectively. To date, there has been 288 days of Advanced LIGO and Virgo observing time. Two or more instruments were observing during 171 days. There were only 15.2 days of full LIGO-Hanford, LIGO-Livingston, and Virgo joint observing. O2 was the first time that Virgo has conducted joint observing with the LIGO observatories since initial LIGO (Abbott et al. 2016a). The Virgo instrument significantly surpassed the average BNS range during the last VSR2/3 science run (~ 10 Mpc) (Abadie et al. 2012) to achieve an average of 27 Mpc during the joint observing period of O2. While the amount of triple-detector observing time is limited during the first two observing runs, the ongoing third observing run will considerably improve the availability of three-detector joint observing time. The methods demonstrated here will be applicable to future analysis of the O3 multi-detector dataset.

We note that there is $\sim$ 117 days of single-detector observing time. In this work we do not focus on the detection of gravitational-wave mergers during this time, however, methods for assigning meaningful significance to such events has been proposed (Callister et al. 2017) and will be investigated in future work. Single-detector observing time has been used in follow-up analyses where a merger could be confirmed by electromagnetic observations (Nitz et al. 2019b; Abbott et al. 2019c).

3. SEARCH FOR BINARY MERGERS

We use a matched-filtering approach as implemented in the open source PyCBC library (Usman et al. 2016; Allen 2005; Nitz et al. 2018). This toolkit has been similarly employed in LIGO/Virgo collaboration and independent analyses (Abbott et al. 2019a; Nitz et al. 2019a). We extend the approach used in the 1-OGC analysis (Nitz et al. 2019a) to handle the analysis of Virgo data. We also incorporate improvements to the ranking of candidates by accounting for time variations in the power spectral density and network sensitivity.

The essential procedure can be summarized as follows. The data from each detector is correlated against a set of possible merger signals. Matched filtering is used to calculate a signal-to-noise (SNR) time series for each potential signal waveform. Our analysis identifies peaks in these time series and follows up the peaks with a set of signal consistency tests. These single-detector candidates are then combined into multi-detector candidates by enforcing astrophysically consistent time delays between detectors, as well as enforcing identical component masses and spins. Finally, these candidates are ranked by the ratio of their signal and noise model likelihoods (see Sec. 3.3).

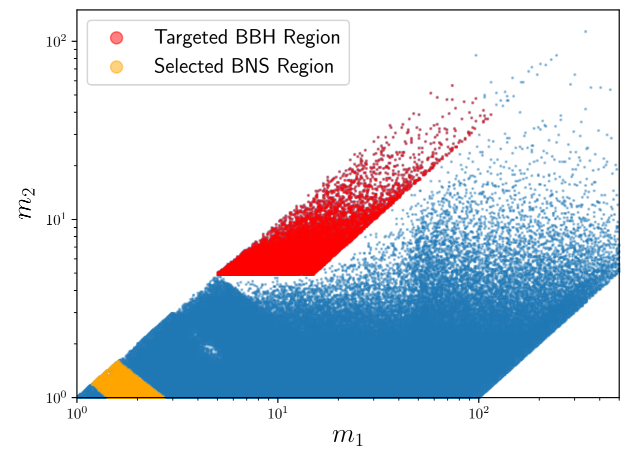

Figure 2. The component masses of templates used to search for compact binary mergers. Templates which define the targeted-binary black hole region are colored in red. Candidates which fall in the selected BNS-like region are discussed in 4.2.

3.1. *Search Space*

Our analysis targets a wide range of BNS, NSBH, and BBH mergers. We perform a matched filter on the data with waveform models that span the range of desired detectable sources. Although the space of possible binary component masses and spins is continuous, we must select a discrete set of points in this space as templates to correlate against the data: we use the set of $\sim 400,000$ templates introduced in Dal Canton & Harry (2017) which has been previously used in Nitz et al. (2019a) and Abbott et al. (2019a). This bank of templates is suitable for the detection of mergers up to binary masses of several hundred solar masses, under the conditions that the dominant gravitational-wave emission mode is adequate to describe the signal and that the effects of precession caused by misalignment of the orbital and component object angular momenta can be neglected Dal Canton & Harry (2017). Fig. 2 shows the distribution of template detector-frame component masses. We use the spinning effective-one-body model (SEOBNRv4) for templates corresponding to mergers with (redshifted, detector frame) total mass $m_1 + m_2 > 4\,M_\odot$ (Taracchini et al. 2014; Bohé et al. 2016). The TaylorF2 post-Newtonian model is used in all other cases (Sathyaprakash & Dhurandhar 1991; Droz et al. 1999; Blanchet 2002; Faye et al. 2012).

3.2. *Single-detector Candidates*

The first stage of our analysis is to identify single-detector candidates. These correspond to peaks in the SNR time series of a particular template waveform. Each is assigned a ranking statistic as we'll discuss be-low. In this work, we do not explicitly conduct a search for sources which only appear in a single detector. However, a ranking of single-detector candidates forms the first stage of our analysis. For each template waveform and detector dataset we calculate a signal-to-noise time series $\rho(t)$ using matched filtering. This can be expressed using a frequency-domain convolution as

$$\rho(t) = 4\Re \int_{f_l}^{f_h} \frac{\tilde{h}^*(f)\tilde{s}(f)}{S_n(f)} e^{2\pi i f t}\, df, \tag{1}$$

where $\tilde{h}$ is the normalized (Fourier domain) template waveform and $\tilde{s}$ is the detector data. S_n is the noise power spectral density (PSD) of the data which is estimated using Welch's method. Peaks in the SNR time series (single-detector candidates) are collected. To control the rate of single-detector candidates to be examined, our analysis pre-clusters these triggers. Only those which are the amongst the loudest 100 every ~ 1 s within a set of predefined chirp-mass bins are kept. The binning ensures that loud triggers from a specific region (which may be caused by non-Gaussian noise artifacts) do not cause quiet signals elsewhere in parameter space to be missed.

We remove candidates where the instrument state indicates the data may be adversely affected by instrumental or environment noise artefacts as indicated by the Gravitational-Wave Open Science Center (GWOSC) (Abbott et al. 2016b, 2018; Vallisneri et al. 2015). However, there remain classes of transient non-Gaussian noise in the LIGO data which produce triggers with large values of SNR (Nuttall et al. 2015; Abbott et al. 2016b, 2018; Cabero et al. 2019). The surviving single-detector candidates are subjected to the signal consistency tests introduced in Allen (2005) and Nitz (2018). These tests check that the accumulation of signal power as a function of frequency, and power outside the expected signal band, respectively, are consistent with an astrophysical explanation. They produce two statistic values which are χ^2 distributed: χ^2_r and $\chi^2_{r,sg}$ respectively. These are used to re-weight (Babak et al. 2013) the single-detector signal strength in two stages. This re-weighting allows candidates which well match an expected astrophysical source to be assigned a statistic value similar to their matched filter SNR, while down-weighting many classes of non-Gaussian noise transients. For all candidates we apply

$$\tilde{\rho} = \begin{cases} \rho, & \text{for } \chi^2_r \leq 1 \\ \rho \left[\frac{1}{2}\left(1 + \left(\chi^2_r\right)^3\right)\right]^{-1/6}, & \text{for } \chi^2_r > 1. \end{cases} \tag{2}$$

For single-detector candidates in templates with (detector-frame) total mass greater than $40\mathrm{M}_\odot$ the statistic is further re-weighted as

$$\hat{\rho} = \begin{cases} \tilde{\rho}, & \text{for } \chi^2_{r,sg} \leq 4 \\ \tilde{\rho}(\chi^2_{r,sg}/4)^{-1/2}, & \text{for } \chi^2_{r,sg} > 4. \end{cases} \tag{3}$$

The latter test is only applied to these short duration, higher mass signals as the test is computationally slow and has has the greatest impact for short duration signals which may be otherwise confused with some classes of transient non-Gaussian noise (Nitz 2018; Cabero et al. 2019). Otherwise, we set $\hat{\rho} = \tilde{\rho}$.

This statistic $\hat{\rho}$ is the same used in the 1-OGC analysis (Nitz et al. 2019a) and LVC O2 catalog Abbott et al. (2019a). We further improve upon this by accounting for rapid changes in the overall PSD estimate. The issue of PSD variation was also addressed in Venumadhav et al. (2019a). Previously we modeled the PSD for each detector as a function of frequency $S_n(f)$, which is estimated on a 512 second timescale. We now introduce a time-dependent factor $v_S(t)$ which accounts for short-term O(10s) variations in sensitivity. We estimate this short term variation using the method described in Mozzon et al. (2019). These short term variation in the PSD will introduce variation in ρ as we use the estimated PSD $S(f)$ to calculate it. The estimated PSD over short time scales $S_s(f)$ can be different from a PSD estimated over a longer duration $S_l(f)$ if the noise is non stationary. In the absence of a signal, the variance of ρ can be calculated as,

$$\langle \rho^2 \rangle = \left[\int_{f_l}^{f_h} \frac{|h(f)|^2}{S_s(f)}\, df\right]^{-1} \int_{f_l}^{f_h} \frac{|h(f)|^2}{S_s(f)} \frac{S_l(f)}{S_s(f)}\, df, \tag{4}$$

Variance is equal to 1 if $S_s(f) = S_l(f)$ To calculate the expected variance of the SNR, we use a filter $F(f) = \mathcal{N}|h(f)|/S_s(f)$, where $\mathcal{N}$ is a normalization constant. Using Parseval's theorem, we can then compute the variation in the PSD as

$$v_S(t_0) = \int_{t_0-\Delta t/2}^{t_0+\Delta t/2} |\mathcal{F}(t) * d(t)|^2\, dt \tag{5}$$

After getting $v_S(t)$, we consider the rate of noise triggers above a given statistic threshold $R_N(> \hat{\rho}_t)$, where the statistic $\hat{\rho}$ is proportional to the SNR obtained by matched filtering using the long-duration PSD $S_l(f)$. The noise trigger rate will vary over time due to the non-stationarity of the PSD and is thus a function of the short-duration PSD variation measure. Since SNR scales as $1/\sqrt{S(f)}$, we naively expect the noise trigger rate to be a function of the 'corrected' SNR $\hat{\rho}/\sqrt{v_S}$; in reality we find a weaker dependence which we write as

$$R_N(> \hat{\rho}_t) = f_N(\hat{\rho}_t v_S(t)^{-\kappa}). \tag{6}$$

Here f_N is a fitting function for the expected noise distribution. Empirically we find, for data without strong non-Gaussian transients (glitches), $f_N(\hat{\rho}) \simeq \exp(-\alpha\hat{\rho}^2/2)$ with $\alpha \simeq 1$.

If we consider small variations of $v_S(t)$ around unity, $v_S(t) = 1 + \epsilon_S$, the logarithm of the trigger rate above threshold will vary as an approximately linear function of ϵ_S:

$$\ln(R_N(> \hat{\rho}_t)) \simeq \text{const.} - \frac{\alpha}{2}\hat{\rho}_t^2 + \alpha\kappa\hat{\rho}_t^2\epsilon_S \tag{7}$$

By determining the slope of the linear log-rate *vs.* v_S dependence for various thresholds $\hat{\rho}$ we estimate a 'corrected' statistic such that the rate of noise triggers above a given threshold remain constant as a function of v_S

$$\hat{\rho} \rightarrow \hat{\rho} v_S(t)^{-0.33} \tag{8}$$

where the constant 0.33 is the numerically tuned scaling factor.

The analysis of Venumadhav et al. (2019a) included a similar correction factor and Zackay et al. (2019) indicates a modest improvement in sensitivity for the sources they consider. We find that in our analysis, the greatest improvement is for sources corresponding to long-duration templates (BNS and NSBH) while there is negligible improvement for the shorter-duration BBH sources.

3.3. *Multi-detector Coincident Candidates*

In the previous section, we discussed how we identify single-detector candidates and assign them a ranking statistic. We now combine single-detector candidates from multiple detectors to form multi-detector candidates (Davies, Gareth et al. 2019). We introduce a new ranking statistic formed from models of the relative signal and noise likelihoods for a particular candidate.

Our signal model is composed of two parts. First, the overall network sensitivity of the analysis at the time of the candidate. We approximate this by using the instantaneous sensitive range of the least sensitive instrument contributing to the multi-detector candidate for a given template (labelled by i), $\sigma_{\min,i}$, relative to a representative range over the analysis, $\bar{\sigma}_i$, for that template. The second part is the probability, given an isotropic and volumetric population of sources, that an astrophysical signal would be observed to have a particular set of parameters defined by $\vec{\theta}$, including time delays, relative amplitudes, and relative phases between the network of observatories. This probability distribution $p(\vec{\theta}|S)$ is calculated by a Monte Carlo method similarly to Nitz et al. (2017). For this work we have extended this technique to three detectors for the first time. Combined, our model for the density of signals recovered with network parameters $\vec{\theta}$ in a combination of instruments characterized by $\sigma_{min,i}$ can be expressed as

$$R_{S,i}(\vec{\theta}) = \left(\frac{\sigma_{\min,i}}{\bar{\sigma}_i}\right)^3 p(\vec{\theta}|S). \tag{9}$$

The noise model is calculated in the same manner as in Nitz et al. (2017). We treat the noise from each detector as being independent and fit our single-detector ranking statistic to an exponential slope. This fit is performed separately for each template. The fit parameters (such as the slope and overall amplitude of the exponential) are initially noisy due to low number statistics, so they are smoothed over the template space using a three-dimensional Gaussian kernel in the template duration, effective spin $\chi_{\rm eff}$, and symmetric mass ratio η parameters. The rate density of noise events with contributing detectors labelled by n can be summarized as

$$R_{N,i}(\{\tilde{\rho}_n\}) = A_{\{n\}} \prod_n r_{n,i} e^{-\alpha_{n,i}\tilde{\rho}_n}, \tag{10}$$

where $r_{n,i}$ and α_i are the overall amplitude and slope of the exponential model of the rate of candidate events from the $i^{\rm th}$ template. The initial factor $A_{\{n\}}$ is the time window for which coincidences can be formed, which depends on the combination of detectors $\{n\}$ being considered. The three-detector coincidence rate is vastly reduced compared to the two-detector rate; in a representative stretch of O2 data, the HLV coincidence rate is found to be around a factor of 10^4 lower than that in HL coincidences. Details of both the signal and noise model calculations will be provided in Davies, Gareth et al. (2019).

The ranking statistic for a given candidate in template i is the log of the ratio of these two rate densities:

$$\tilde{\Lambda} = \log(R_{S,i}/R_{N,i}) + \text{const.}, \tag{11}$$

where we drop the dependences on $\vec{\theta}$ and $\{\tilde{\rho}_n\}$ for simplicity of notation. Typically, one signal event (or loud noise event) in the gravitational-wave data stream may give rise to a large number of correlated candidate multi-detector events within a short time, in different templates and with different combinations of detectors $\{n\}$. To calculate the significance of such a 'cluster' of events, we will approximate their arrival as a Poisson process: in order to do this, we keep the event from each cluster with highest $\tilde{\Lambda}$ — typically the highest-ranked event within a 10 s time window — and discard the rest. If we compare this new statistic to the one employed for the 1-OGC analysis (Nitz et al. 2019a) using a simulated population of both BNS and BBH mergers, we find an 8% increase in the detectable volume during the O1 period at a fixed false alarm rate. In addition to this improved sensitivity for events where H1 and L1 contribute, this search will also benefit by analyzing times where Virgo and only one LIGO detector are operating (as in Table 1), and also by improved sensitivity in times when all three detectors are operating, due to the ability to form 3-detector events. Such sensitivity improvements are detailed in Davies, Gareth et al. (2019).

3.4. *Statistical Significance*

In the previous section we introduce the ranking statistic used in our analysis. We empirically measure the statistical significance of a particular value of our ranking statistic by comparing it to a set of false (noise) candidate events produced in numerous fictitious analyses. Each such analysis is generated by time-shifting the data from one detector by an amount greater than is astrophysically allowed by light travel time considerations Babak et al. (2013); Usman et al. (2016). By construction, the results of these analyses cannot contain true multi-detector astrophysical candidates. Otherwise, each time-shifted analysis is treated in the identical manner as the search itself. By repeating this procedure, upwards of 10^4 years' worth of false alarms can be produced from just a few days of data. This method has been employed to detect significant events in numerous analyses (Nitz et al. 2019a; Abbott et al. 2019a; Venumadhav et al. 2019b; Abadie et al. 2012; Abbott et al. 2009). The validity of the resulting background estimate follows from an assumption that the times of occurrence of noise events are statistically independent between different detectors (see Was et al. (2010); Capano et al. (2017) for further discussion of the time shift method and empirical background estimation in general). This is a reasonable assumption for detectors separated by thousands of kilometres (Abbott et al. 2016b). The time shift method has the advantage that no other assumptions about the noise need be accurate: the populations and morphology of noise artefacts need not be uncorrelated or different between detectors, only the times at which they occur. In fact the LIGO and Virgo instruments share common components and environmental coupling mechanisms which may produce similar classes of non-Gaussian artefacts.

3.5. *Targeting Binary Black Hole Mergers*

Given a population of individually significant BBH mergers, it is possible to incorporate knowledge about the overall distribution and rate of sources to identify weaker candidates. A similar approach was employed in Nitz et al. (2019a) and is the basis of astrophysical significance statements in Abbott et al. (2019a). In this catalog we improve over the strategy of Nitz et al. (2019a) which considered an excessively conservative parameter space for BBH and did not use an explicit model of the distribution of signals and noise within that space. In addition, we restrict to sources which are consistent with our signal models by imposing a threshold on our primary signal consistency test to reject any single-detector candidate with $\chi_r > 2.0$. Simulated signals within our target population, and the individual highly significant candidates previously detected are consistent with this choice. (The full, non-BBH-specific analysis allows a much greater deviation from our signal models before rejection of a candidate.)

As a first step in obtaining the targeted BBH results we restrict the analysis to a sub-space of the full search, illustrated in Fig. 2. Rather than applying this constraint *after* obtaining the set of 'clustered' candidates via selecting the highest ranked event within 10 s windows, as in Nitz et al. (2019a), here we apply the constraint to candidates *prior* to the clustering step. This allows us to choose a less extensive BBH region containing fewer templates than employed in Nitz et al. (2019a) without loss of sensitivity. (The previous method used a wider BBH template set to allow for the possibility that a signal inside the intended target region is recovered only by a template lying outside that region, due to clustering.) Our BBH region is specified by $m_{1,2} > 5\mathrm{M}_{\odot}$, $1/3 < m_1/m_2 < 3$, and $\mathcal{M} < 60$. The upper boundary is consistent with the redshifted detector-frame masses that would be obtained by the observed highest-mass sources near detection threshold.

Applying a prior over the intrinsic parameters of the distribution of detectable sources was proposed in Dent & Veitch (2014) and tested in Nitz et al. (2017). In this work, we impose an explicit detection prior that is flat over chirp mass. As seen in Fig. 2, the distribution of templates is highly non-uniform. The BBH region of template is placed first using a stochastic algorithm (Dal Canton & Harry 2017; Ajith et al. 2014), where density of templates directly correlates to density of effectively independent noise events. The template density over $\mathcal{M}$ scales as $\mathcal{M}^{-11/3}$, which we verify empirically for our bank. Our detection statistic aims to follow the relative rate density of signal vs. noise events at fixed SNR, and we make the simple choice of assuming a signal density flat over $\mathcal{M}$: thus the ranking statistic receives an extra term describing the ratio of signal to noise densities over component masses:

$$\tilde{\Lambda}_{\mathrm{BBH}} = \tilde{\Lambda} + \frac{11}{3} \ln\left(\frac{\mathcal{M}}{\mathcal{M}_f}\right), \tag{12}$$

Table 2. Candidate events in the full search of O1 and O2 data. Candidates are sorted by FAR evaluated for the entire bank of templates. Note that ranking statistic and false alarm rate may not have a strictly monotonic relationship due to varying data quality between sub-analyses. The mass and spin parameters listed are associated with the template waveform yielding the highest ranked multi-detector event for each candidate, and may differ significantly from full Bayesian parameter estimates. Masses are quoted in detector frame, and are thus larger than source frame masses by a factor $(1 + z)$, where z is the source redshift.

Date designation	GPS time	FAR^{-1} (y)	Detectors	$\tilde{\Lambda}$	ρ_H	ρ_L	ρ_V	m_1	m_2	$\chi_{\rm eff}$
170817+12:41:04UTC	1187008882.45	> 10000	HL	180.46	18.6	24.3	-	1.5	1.3	-0.00
150914+09:50:45UTC	1126259462.43	> 10000	HL	93.82	19.7	13.4	-	44.2	32.2	0.09
170104+10:11:58UTC	1167559936.60	> 10000	HL	35.54	9.0	9.6	-	47.9	16.0	0.03
170823+13:13:58UTC	1187529256.52	> 10000	HL	55.04	6.3	9.2	-	68.9	47.2	0.23
170814+10:30:43UTC	1186741861.54	> 10000	HL	52.85	9.0	13.0	-	58.7	23.3	0.53
151226+03:38:53UTC	1135136350.65	> 10000	HL	42.90	10.7	7.4	-	14.8	8.5	0.24
170809+08:28:21UTC	1186302519.76	9400	HL	40.59	6.6	10.7	-	36.0	33.7	0.07
170608+02:01:16UTC	1180922494.49	> 910[a]	HL	51.01	12.5	8.7	-	16.8	6.1	0.31
151012+09:54:43UTC	1128678900.45	220	HL	20.18	7.0	6.7	-	30.8	12.9	-0.05
170729+18:56:29UTC	1185389807.33	6.4	HL	15.33	7.4	6.7	-	106.5	49.7	0.59
170121+21:25:36UTC	1169069154.58	1.3	HL	15.76	5.1	8.7	-	40.4	13.6	-0.98
170727+01:04:30UTC	1185152688.03	.53	HL	13.75	4.5	6.9	-	65.2	26.5	-0.35
170818+02:25:09UTC	1187058327.09	.22	HL	13.29	4.4	9.4	-	53.7	27.4	0.07
170722+08:45:14UTC	1184748332.91	.11	HL	12.19	5.0	6.4	-	248.1	7.1	0.99
170321+03:13:21UTC	1174101219.23	.1	HL	12.22	6.5	6.4	-	11.0	1.3	-0.89
170310+09:30:52UTC	1173173470.77	.07	HL	12.15	6.1	6.2	-	2.1	1.1	-0.20
170809+03:55:52UTC	1186286170.08	.07	LV	7.34	-	7.0	5.1	6.2	1.2	0.60
170819+07:30:53UTC	1187163071.23	.05	HV	11.35	6.3	-	6.7	135.2	2.5	0.85
170618+20:00:39UTC	1181851257.72	.05	HL	11.49	5.2	6.7	-	2.9	2.1	0.30
170416+18:38:48UTC	1176403146.15	.04	HL	11.21	5.1	6.9	-	7.8	1.1	-0.47
170331+07:08:18UTC	1174979316.31	.04	HL	11.03	5.2	7.0	-	3.9	1.1	-0.34
151216+18:49:30UTC	1134326987.60	.04	HL	11.54	6.1	6.0	-	13.9	5.0	-0.41
170306+04:45:50UTC	1172810768.08	.04	HL	11.47	4.8	7.3	-	26.4	1.8	0.23
151227+16:52:22UTC	1135270359.27	.04	HL	11.75	7.3	4.6	-	154.5	4.9	1.00
170126+23:56:22UTC	1169510200.17	.04	HL	11.61	6.4	5.7	-	4.9	1.3	0.79
151202+01:18:13UTC	1133054310.55	.03	HL	11.48	6.5	5.7	-	40.4	1.8	-0.26
170208+20:23:00UTC	1170620598.15	.03	HL	11.12	6.8	5.4	-	6.9	1.0	0.09
170327+17:07:35UTC	1174669673.72	.03	HL	10.65	6.0	6.2	-	40.1	1.0	0.97
170823+13:40:55UTC	1187530873.86	.03	LV	9.30	-	8.0	5.8	117.9	1.3	0.98
150928+10:49:00UTC	1127472557.93	.03	HL	11.28	6.0	6.3	-	2.5	1.0	-0.70

[a]The FAR is limited only by the available background data. A short analysis period is used for the 170608 data which was released separately due to an instrument angular control procedure affecting data from the Hanford observatory (Abbott et al. 2017b).

where $\mathcal{M}_f = 20\,\mathrm{M}_\odot$ is a fiducial reference mass scale. Roughly, any given lower-mass template is less likely to detect a signal than a higher-mass template given that templates are much sparser at high masses.

Our choice of BBH region and detection prior has a similar effect as the highly constrained search space and multiple chirp mass bins used in Venumadhav et al. (2019b) but avoids the multiple boundary effects present there and provides a more clearly implemented and astrophysically motivated prior distribution. Furthermore, our method provides a path forward to more accurate assessment of lower-SNR candidates as our understanding of the overall population evolves.

To estimate the probability $p_{\rm astro}$ that a given candidate is astrophysical in origin we combine the background of this targeted BBH analysis with the estimated distribution of observations. We improve upon the analysis in Nitz et al. (2019a) which employed an analytic model of the signal distribution and a fixed conservative rate of mergers by using the mixture model method developed in Farr et al. (2015) and similar to that employed in Abbott et al. (2019a). This method requires the distribution of noise and signals over our ranking statistic, which we take from our time-slide background estimates and a population of simulated signals respectively.[2]

Using a simulated set of BBH mergers, we find that the targeted BBH analysis recovers a factor 1.5–1.6 more sources at a fixed false alarm rate than the full parameter space analysis. This change in sensitivity is attributed partly to the inclusion only of background events consistent with BBH mergers, and partly to the choice of ranking statistic to optimize sensitivity to a nominal BBH signal population.

4. OBSERVATIONAL RESULTS

We present compact binary merger candidates from the complete set of public LIGO and Virgo data spanning the observing runs from 2015-2017. This comprises roughly 171 days of multi-detector observing time which we divide into 31 sub-analyses. Except as noted, each analysis contains ~ 5 days of observing time which allows for estimation of the false alarm rate to < 1 per 10,000 years. This interval allows us to track changes in the detector configuration which may result in time-changing detector quality. All data was retrieved from GWOSC Vallisneri et al. (2015), and we have used the most up-to-date version of bulk data released. We note that an exceptional data release was produced by GWOSC which contains background data relating to GW170608. We have incorporated this into its own sub-analysis to preserve consistent data quality.

The top candidates sorted by FAR from the complete analysis are given in Table 2. All of the most significant candidates were observed by LIGO-Hanford and LIGO-Livingston which are the two most sensitive detectors in the network and contribute the bulk of the observing time. There are 8 BBH and 1 BNS candidates at a FAR less than 1 per 100 years. These sources are confidently detected in the full analysis without optimizing the search for any specific population of sources. The most significant following candidates represent GW170729, GW170121, GW170727 and GW170818 respectively. A similar PyCBC-based analysis was performed in Abbott et al. (2019a) but used a higher single-detector SNR threshold than employed in our analysis ($\rho > 5.5$ vs 4.0); as the latter three events were found with $\rho <= 5.1$ in the LIGO-Hanford detector, we would not expect this earlier analysis to identify them.

[2] We use the Laguerre-Gauss integral method described in Creighton (2017) to marginalize over the Poisson rate of signals in the calculation of $p_{\rm astro}$ values.

4.1. *Binary Black Holes*

Using the targeted BBH analysis introduced in Sec. 3.5 we report results for BBH mergers consistent with the existing set of highly significant merger events. The probability that a candidate is astrophysical in origin, $p_{\rm astro}$, is calculated for the most significant candidates. Our analysis identifies 14 BBH candidates with $p_{\rm astro} > 50\%$ meeting the standard detection criteria introduced in Abbott et al. (2019a) and similarly followed in Venumadhav et al. (2019b). Our results are broadly consistent with the union of those two analyses as our candidate list includes all prior claimed BBH detections. We confirm the observation of GW170121, GW170304, and GW170727 reported in Venumadhav et al. (2019a) as significant. We also report the marginal detection of GW151205, which corresponds to a heavy binary black hole merger that may be more massive than GW170729.

Several marginal events reported in Venumadhav et al. (2019b,a) are found as top candidates, but do not meet our detection threshold based on estimated probability of astrophysical origin. Numerous differences between these two analyses including template bank placement, treatment of data, choice of signal consistency test, and method for assigning astrophysical significance may be the cause of reported differences. The consistency of results for less marginal candidates indicates that differences in analysis sensitivity are likely marginal. Cross comparison with a common set of simulated signals would be required for a more definite assessment.

Future analyses incorporating more sophisticated treatment of the source distribution may yield different results for the probability of astrophysical origin for some sub-threshold candidates. For example 151216+09:24:16UTC, which was first identified in Nitz et al. (2019a) and is now assigned a $p_{\rm astro} \sim 0.2$, could obtain a higher probability of being astrophysical under a model with a distribution of detected mergers peaked close to its apparent component masses, rather than uniform over $\mathcal{M}$ as taken here. In any case the astrophysical probability we assign assumes that the candidate event, if astrophysical, is drawn from an existing population. The prior applied here to the population distribution over component masses could be extended to the distribution over component-object spins. (Here, we implicitly apply a prior over spins which mirrors the density of templates, which is not far from uniform over $\chi_{\rm eff}$.) As 151216+09:24:16UTC may have high component spins, if the set of highly significant observations does not include any comparable systems its probability of astrophysical origin could be arbitrarily small, depending on a choice of prior distribution over spins.

Table 3. Candidates from the targeted binary black hole sub-region sorted by the probability they are astrophysical in origin. As in Table 2, the mass and spin parameters listed are associated with the template waveform yielding the highest ranked multi-detector event for each candidate; component masses are stated in detector frame and are thus redshifted relative to source masses.

Date designation	GPS time	$p_{\rm astro}$	FAR^{-1} (y)	Detectors	$\tilde{\Lambda}_{\rm BBH}$	ρ_H	ρ_L	ρ_V	m_1	m_2	$\chi_{\rm eff}$
150914+09:50:45UTC	1126259462.43	> 0.999	> 10000	HL	111.71	19.7	13.4	-	44.2	32.2	0.09
170814+10:30:43UTC	1186741861.53	> 0.999	> 10000	HL	61.58	9.3	13.8	-	47.9	16.0	0.03
170823+13:13:58UTC	1187529256.52	> 0.999	> 10000	HL	59.43	6.3	9.2	-	68.9	47.2	0.23
170104+10:11:58UTC	1167559936.60	> 0.999	> 10000	HL	47.32	9.1	9.9	-	38.4	18.2	-0.24
151226+03:38:53UTC	1135136350.65	> 0.999	> 10000	HL	40.58	10.7	7.4	-	14.8	8.5	0.24
151012+09:54:43UTC	1128678900.45	> 0.999	> 10000	HL	20.25	7.0	6.7	-	30.8	12.9	-0.05
170809+08:28:21UTC	1186302519.76	> 0.999	8300[a]	HL	43.34	6.6	10.7	-	36.0	33.7	0.07
170729+18:56:29UTC	1185389807.33	> 0.999	4000	HL	19.16	7.5	7.1	-	68.9	47.2	0.23
170608+02:01:16UTC	1180922494.49	> 0.999	> 910	HL	55.12	12.5	8.7	-	16.8	6.1	0.31
170121+21:25:36UTC	1169069154.58	> 0.999	210[a]	HL	23.86	5.1	8.9	-	46.1	27.9	-0.17
170818+02:25:09UTC	1187058327.09	> 0.999	5.1[a]	HL	21.42	4.4	9.4	-	53.7	27.4	0.07
170727+01:04:30UTC	1185152688.03	0.994	180	HL	15.84	4.5	6.9	-	65.2	26.5	-0.35
170304+16:37:53UTC	1172680691.37	0.70	2.5	HL	11.61	4.6	7.1	-	68.9	47.2	0.23
151205+19:55:25UTC	1133380542.42	0.53	.61	HL	10.97	5.8	4.8	-	107.8	36.9	0.42
151217+03:47:49UTC	1134359286.35	0.26	.15	HL	9.61	6.7	5.6	-	40.0	14.8	0.84
170201+11:03:12UTC	1169982210.74	0.24	.16	HL	9.26	6.0	5.6	-	73.7	25.1	0.91
170425+05:53:34UTC	1177134832.19	0.21	.2	HL	9.42	5.1	5.8	-	76.1	25.6	-0.17
151216+09:24:16UTC	1134293073.19	0.18	.1	HL	9.25	5.9	5.5	-	41.8	34.3	0.91
170202+13:56:57UTC	1170079035.73	0.13	.06	HL	8.37	5.0	6.6	-	40.0	14.5	-0.32
170104+21:58:40UTC	1167602338.72	0.12	.03	HL	8.80	5.6	5.4	-	91.5	30.8	0.99
170220+11:36:24UTC	1171625802.53	0.10	.05	HL	8.43	4.4	5.2	-	107.8	36.9	0.42
170123+20:16:42UTC	1169237820.55	0.08	.04	HL	7.97	5.0	5.3	-	50.5	31.9	-0.73
151011+19:27:49UTC	1128626886.61	0.08	.12	HL	8.45	4.9	6.6	-	67.5	32.5	0.15
151216+18:49:30UTC	1134326987.60	0.07	.03	HL	8.14	6.1	6.0	-	13.9	5.0	-0.41
170721+05:55:13UTC	1184651731.37	0.06	.04	HL	7.76	6.6	5.1	-	46.0	18.6	-0.10
170403+23:06:11UTC	1175295989.23	0.03	.07	HL	7.26	5.2	5.2	-	76.1	25.6	-0.17
170629+04:13:55UTC	1182744853.11	0.02	.06	HL	6.72	6.6	4.8	-	43.4	14.8	0.98
170620+01:14:02UTC	1181956460.10	0.02	.04	HL	6.18	5.7	5.1	-	48.7	19.6	0.07
170801+23:28:19UTC	1185665317.35	-	.04	LV	8.59	-	6.9	4.3	30.2	12.5	-0.30
170818+09:34:45UTC	1187084103.28	-	.04	HV	8.40	6.5	-	4.4	65.6	22.2	0.92

[a]The false alarm rate is limited by false coincidences arising from the candidate's time-shifted LIGO-Livingston single-detector trigger. If removed from its own background, the FAR is < 1 per 10,000 years.

4.2. *Neutron Star Binaries*

Our analysis identified GW170817 as a highly significant merger, however, no further individually significant BNS nor NSBH mergers were identified. As the population of BNS and NSBH sources is not yet well constrained, we cannot reliably employ the methodology used to detect population consistent BBH candidates. However, BNS candidates especially are prime candidates for the observation of electromagnetic counterparts such as GRBs and kilonovae. It may be possible by correlating with auxiliary datasets to determine if weak candidates are astrophysical in origin. An example is the sub-threshold search of Fermi-GBM and 1-OGC triggers (Nitz et al. 2019b), which defined, based on galactic neutron star observations (Ozel et al. 2012), a likely BNS merger region to span $1.03 < \mathcal{M} < 1.36$ and effective spin $|\chi_{\rm eff}| < 0.2$. This region is highlighted in Fig. 2 and the top candidates are shown in Table 4.

5. DATA RELEASE

We provide supplementary materials online which provide information on each of $\sim 10^6$ sub-threshold candidates (Nitz & Capano 2019). Reported information includes candidate event time, SNR in each observatory, and results of the signal-consistency tests performed.

Table 4. Candidate events with template parameters consistent with BNS mergers sorted by ranking statistic $\tilde{\Lambda}$. The chirp mass $\mathcal{M}$ of the candidate's associated template waveform is given in the detector frame. All candidates here were found by the LIGO-Hanford and LIGO-Livingston observatories.

Date Designation	GPS Time	$\tilde{\Lambda}$	ρ_H	ρ_L	$\mathcal{M}$
170817+12:41:04UTC	1187008882.45	180.46	18.6	24.3	1.20
161217+02:44:33UTC	1165977890.44	10.81	6.2	6.0	1.15
151214+21:03:35UTC	1134162232.89	9.26	6.0	5.7	1.06
151105+20:34:28UTC	1130790885.49	8.97	6.0	6.3	1.29
160103+02:29:54UTC	1135823411.78	8.41	5.3	6.5	1.16
170204+00:34:28UTC	1170203686.48	8.40	5.1	6.4	1.25
170819+11:06:26UTC	1187176004.83	8.37	6.2	6.0	1.06
170213+21:45:15UTC	1171057533.29	8.35	7.4	6.1	1.15
151112+05:48:49UTC	1131342546.36	8.11	5.7	6.4	1.35
150930+12:45:03UTC	1127652320.31	8.10	6.0	5.8	1.15

These candidates cover the full range of binary neutron star, neutron star – black hole, and binary black hole mergers. A separate listing of candidates within the BBH region discussed in Sec. 3.5 is also provided. The top of these candidates include estimates of their astrophysical significance p_{astro}. To help distinguish between these large number of candidates, the ranking statistic we've developed along with an estimate of the false alarm rate is also provided for every event. Configuration files for the analyses performed in additional to analysis metadata are also provided.

6. CONCLUSIONS

We have reported the 2-OGC catalog of gravitational-wave candidates from compact-binary coalescences which spans the full range of binary neutron star, neutron star–black hole, and binary black hole mergers. Our work represents an analysis of the complete set of LIGO and Virgo public data which spans the observing runs from 2015-2017. A third observing run (O3) began in April, 2019 Abbott et al. (2016a). Alerts for several dozen merger candidates have been issued to date during this run[3]. The first half of the run (O3a) ended on Oct 1 2019 with a planned release of the corresponding data in Spring 2021. As the data is not yet released, the catalog here covers only the first two observing runs.

We use a matched-filtering, template-based approach to identify candidates and improve over the 1-OGC analysis (Nitz et al. 2019a) by incorporating corrections for time variations in power spectral density estimates and network sensitivity. Furthermore, we have demonstrated extending a PyCBC-based analysis to handle data from more than two detectors. The 2-OGC catalog contains the most comprehensive set of merger candidates to date, including 14 BBH mergers with $p_{\mathrm{astro}} > 50\%$ along with the single BNS merger GW170817. We independently confirm many of the results of Abbott et al. (2019a) and Venumadhav et al. (2019b). We find no additional individually significant BNS or NSBH mergers, however, we provide our full set of sub-threshold candidates for further analysis(Nitz & Capano 2019).

We acknowledge the Max Planck Gesellschaft and the Atlas cluster computing team at AEI Hannover for support. Research supported by Maria de Maeztu Unit of Excellence MDM-2016-0692. This research was supported in part by the National Science Foundation under Grant No. NSF PHY-1748958. This research has made use of data, software and/or web tools obtained from the Gravitational Wave Open Science Center (https://www.gw-openscience.org), a service of LIGO Laboratory, the LIGO Scientific Collaboration and the Virgo Collaboration. LIGO is funded by the U.S. National Science Foundation. Virgo is funded by the French Centre National de Recherche Scientifique (CNRS), the Italian Istituto Nazionale della Fisica Nucleare (INFN) and the Dutch Nikhef, with contributions by Polish and Hungarian institutes.

[3] https://gracedb.ligo.org/superevents/public/O3

REFERENCES

Aasi, J., et al. 2015, Class. Quantum Grav., 32, 074001, doi: 10.1088/0264-9381/32/7/074001

Abadie, J., et al. 2012, Phys. Rev., D85, 082002, doi: 10.1103/PhysRevD.85.082002

Abbott, B., et al. 2009, PhRvD, 80, 047101

Abbott, B. P., et al. 2016a, Living Rev. Relat., 19, 1, doi: 10.1007/lrr-2016-1

—. 2016b, Class. Quant. Grav., 33, 134001, doi: 10.1088/0264-9381/33/13/134001

—. 2017a, Astrophys. J., 848, L12, doi: 10.3847/2041-8213/aa91c9

—. 2017b, Astrophys. J., 851, L35, doi: 10.3847/2041-8213/aa9f0c

—. 2018, Class. Quant. Grav., 35, 065010, doi: 10.1088/1361-6382/aaaafa

—. 2019a, Phys. Rev., X9, 031040, doi: 10.1103/PhysRevX.9.031040

—. 2019b, Astrophys. J., 882, L24, doi: 10.3847/2041-8213/ab3800
—. 2019c. https://arxiv.org/abs/1907.01443
Acernese, F., et al. 2015, Class. Quantum Grav., 32, 024001, doi: 10.1088/0264-9381/32/2/024001
Ajith, P., Fotopoulos, N., Privitera, S., Neunzert, A., & Weinstein, A. J. 2014, Phys. Rev. D, 89, 084041, doi: 10.1103/PhysRevD.89.084041
Allen, B. 2005, Phys. Rev. D, 71, 062001, doi: 10.1103/PhysRevD.71.062001
Andreoni, I., et al. 2018. https://arxiv.org/abs/1812.03161
Antelis, J. M., & Moreno, C. 2018. https://arxiv.org/abs/1807.07660
Babak, S., Biswas, R., Brady, P., et al. 2013, Phys. Rev. D, 87, 024033, doi: 10.1103/PhysRevD.87.024033
Blanchet, L. 2002, Living Rev. Rel., 5, 3
Bohé, A., et al. 2016. https://arxiv.org/abs/1611.03703
Cabero, M., et al. 2019, Class. Quant. Grav., 36, 155010, doi: 10.1088/1361-6382/ab2e14
Callister, T. A., Kanner, J. B., Massinger, T. J., Dhurandhar, S., & Weinstein, A. J. 2017, Class. Quant. Grav., 34, 155007, doi: 10.1088/1361-6382/aa7a76
Capano, C., Dent, T., Hanna, C., et al. 2017, PhRvD, 96, 082002, doi: 10.1103/PhysRevD.96.082002
Countryman, S., Keivani, A., Bartos, I., et al. 2019. https://arxiv.org/abs/1901.05486
Creighton, J. 2017, Certain Identities in FGMC, Tech. Rep. LIGO-T1700029-v1, LIGO
Dal Canton, T., & Harry, I. W. 2017. https://arxiv.org/abs/1705.01845
Davies, Gareth et al. 2019, In preparation
Dent, T., & Veitch, J. 2014, Phys.Rev., D89, 062002, doi: 10.1103/PhysRevD.89.062002
Droz, S., Knapp, D. J., Poisson, E., & Owen, B. J. 1999, PhRvD, 59, 124016
Farr, W. M., Gair, J. R., Mandel, I., & Cutler, C. 2015, PhRvD, 91, 023005, doi: 10.1103/PhysRevD.91.023005
Faye, G., Marsat, S., Blanchet, L., & Iyer, B. R. 2012, Class. Quant. Grav., 29, 175004, doi: 10.1088/0264-9381/29/17/175004
Mozzon, S., Nuttall, L., & Lundgren, A. 2019, In preparation
Nitz, A. H. 2018, Class. Quant. Grav., 35, 035016, doi: 10.1088/1361-6382/aaa13d
Nitz, A. H., Capano, C., Nielsen, A. B., et al. 2019a, Astrophys. J., 872, 195, doi: 10.3847/1538-4357/ab0108
Nitz, A. H., & Capano, C. e. a. 2019, 2-OGC Open Gravitational-wave Catalog, www.github.com/gwastro/2-ogc, GitHub
Nitz, A. H., Dent, T., Dal Canton, T., Fairhurst, S., & Brown, D. A. 2017, Astrophys. J., 849, 118, doi: 10.3847/1538-4357/aa8f50
Nitz, A. H., Nielsen, A. B., & Capano, C. D. 2019b, Astrophys. J., 876, L4, doi: 10.3847/2041-8213/ab18a1
Nitz, A. H., Harry, I. W., Willis, J. L., et al. 2018, PyCBC Software, https://github.com/gwastro/pycbc, GitHub
Nuttall, L. K., et al. 2015, Class. Quantum Grav., 32, 245005, doi: 10.1088/0264-9381/32/24/245005
Ozel, F., Psaltis, D., Narayan, R., & Villarreal, A. S. 2012, Astrophys.J., 757, 55, doi: 10.1088/0004-637X/757/1/55
Sathyaprakash, B. S., & Dhurandhar, S. V. 1991, Phys. Rev. D, 44, 3819, doi: 10.1103/PhysRevD.44.3819
Setzer, C. N., Biswas, R., Peiris, H. V., et al. 2018, doi: 10.1093/mnras/stz506
Taracchini, A., Buonanno, A., Pan, Y., et al. 2014, PhRvD, 89, 061502, doi: 10.1103/PhysRevD.89.061502
Usman, S. A., et al. 2016, Class. Quant. Grav., 33, 215004, doi: 10.1088/0264-9381/33/21/215004
Vallisneri, M., Kanner, J., Williams, R., Weinstein, A., & Stephens, B. 2015, J. Phys. Conf. Ser., 610, 012021, doi: 10.1088/1742-6596/610/1/012021
Venumadhav, T., Zackay, B., Roulet, J., Dai, L., & Zaldarriaga, M. 2019a, Phys. Rev., D100, 023011, doi: 10.1103/PhysRevD.100.023011
—. 2019b. https://arxiv.org/abs/1904.07214
Was, M., Bizouard, M.-A., Brisson, V., et al. 2010, Class. Quantum Grav., 27, 015005, doi: 10.1088/0264-9381/27/1/015005
Zackay, B., Venumadhav, T., Roulet, J., Dai, L., & Zaldarriaga, M. 2019. https://arxiv.org/abs/1908.05644